Desalination 526 (2022) 115548

Contents lists available at ScienceDirect

Desalination

journal homepage: www.elsevier.com/locate/desal

Boron removal by water molecules inside covalent organic framework (COF) multilayers

Xin Zhang [a,b], Mingjie Wei [a,*], Zhe Zhang [a], Xiansong Shi [a], Yong Wang [a,*]

[a] State Key Laboratory of Materials-Oriented Chemical Engineering, College of Chemical Engineering, Nanjing Tech University, Nanjing 211816, Jiangsu, PR China
[b] Jiangsu Key Laboratory of Hazardous Chemicals Safety and Control, College of Safety Science and Engineering, Nanjing Tech University, Nanjing 211816, Jiangsu, PR China

HIGHLIGHTS

- A novel strategy of driving water molecules to reject boron is proposed.
- Rejection mechanism is due to the hydrogen bond interaction between pore and water.
- The COF-TpTG nanopore fulfilled with fluidic water offers excellent water permeance.

GRAPHICAL ABSTRACT

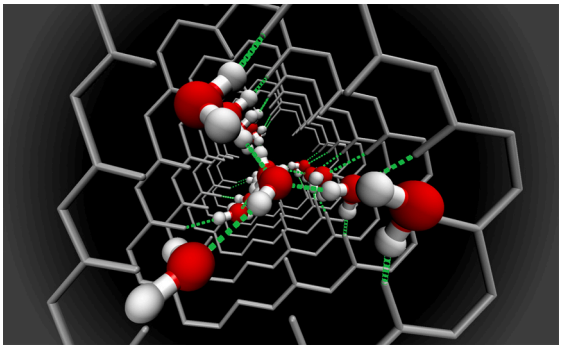

ARTICLE INFO

Keywords:
Boron removal
Covalent organic framework (COF)
Rejection mechanism
Nonequilibrium molecular dynamics
Reverse osmosis

ABSTRACT

Removal of small neutral solutes (SNSs) by reverse osmosis membranes is crucial but challenging. Common consideration of narrowing pore sizes works very little as SNSs have close sizes to the one of water molecules. The most serious drawback of narrowing pore sizes is the reduction of permeance, which dramatically enhances the energy input per volume of permeate water. In this work, an alternative strategy of driving water molecules to reject SNSs is proposed. Using non-equilibrium molecular dynamics simulations, we reveal that inside the nanopores of TpTG multilayers, stable imine-linked covalent organic frameworks, water molecules will preferentially adsorb via the hydrogen bonding interaction. In that way, water molecules in TpTG multilayers other than TpTG themselves can completely reject SNSs, e.g. boric acid. The permeance of TpTG multilayers is excellent as the nanopores are fulfilled with fluidic water. The findings in this work will inspire researchers with an alternative way to design the membranes for SNS removal.

1. Introduction

Over the past few decades, reverse osmosis (RO) technology has gained great success in the desalination market because it is more energy-efficient compared to traditional thermal desalination technologies. Currently, ~70% of the world's installed capacity of desalination

* Corresponding authors.
E-mail addresses: mj.wei@njtech.edu.cn (M. Wei), yongwang@njtech.edu.cn (Y. Wang).

https://doi.org/10.1016/j.desal.2022.115548
Received 14 October 2021; Received in revised form 23 December 2021; Accepted 2 January 2022
Available online 10 January 2022

is provided by RO technology [1]. However, there are some bottlenecks in the prevailingly used polymeric RO membranes. One main challenge is low rejections to the small neutral solutes (SNSs) [2,3].

SNSs refer to the undissociated low-molecular-weight molecules, including boric acid, urea, *N*-nitrosodimethylamine, and trihalomethanes [3,4]. The difficulty to remove SNSs by traditional RO membranes lies on the small size and the poorly hydrated state, resulting in hydrodynamic sizes smaller than those of hydrated ions. SNSs are naturally existing and/or human activity related. Representatively, boric acid is ubiquitously present in seawater. Boric acid ($B(OH)_3$) is a weak acid with pKa = 9.2 and can convert into the borate ion ($B(OH)_4^-$) at high pH. In seawater of pH = 8.4, boron is mainly present in the molecular form of $B(OH)_3$ with an average concentration of 4.5 mg L^{-1} [5].

Although boron is an essential micronutrient, its concentration difference between deficiency and toxicity is very narrow. Excessive exposure can cause detrimental effects to plants, animals, and possibly humans [6,7]. The World Health Organization (WHO) recommends the boron concentration of 2.4 mg L^{-1} for drinking water [8]. Although this guidance value is based on a human health perspective, some countries limit the concentration as low as 0.5 mg L^{-1} to meet the agricultural requirement [9]. To meet this standard, the boron rejection of the RO process should be greater than 90%. Unfortunately, the rejection of current commercial RO membranes is usually lower than 80% [10].

Boron removal often needs improvements by using a two-stage RO system [11] or coupling the RO process with some other techniques, such as pH adjustment [12], pre-adsorption [6], and other processes [13]. These hybrid membrane processes can effectively enhance boron rejection >90% but consume additional energy, chemicals, and capital cost. This consumption will be sharply decreased if single-stage RO membranes with high boron rejections are available.

To improve the boron rejection of RO membranes, researchers focus on modifying the active polyamide layer to enhance the steric hindrance or adjust the membrane affinity to $B(OH)_3$ [14]. The boron rejection could be improved by incorporating some molecular plugs into the active polyamide layer, such as aliphatic amines [15,16], polyisobutylene [17], and 4-nitrobenzenesulfonyl chloride [18]. Another method is the introduction of boron-adsorptive functional groups to enhance boron rejection because the pore occupied by the adsorbed $B(OH)_3$ will slow down the subsequent transport of the boron molecules [19,20]. However, these increased boron rejections are usually at the sacrifice of more than half of the water permeance. The significant decrease in water permeance may be attributed to the decreased effective pore size because of the wide pore size distribution of polymeric RO membranes [21]. Moreover, their free-volume sub-nanometer pores are easy to be affected by the operating factors. For example, increasing the operating temperature will lead to decreased boron rejections [22]. The reason is that the increased temperature will speed up the movement of the polymer chains, which facilitates the passage of $B(OH)_3$ molecules through the membrane.

Alternatively, as an emerging class of crystalline porous polymers, covalent organic frameworks (COFs) possess high porosity as well as regular and structurally designable nanopores, which are one of the ideal membrane materials. It has been predicted that the kinds of COFs are almost half a million [23]. Unfortunately, the current fabrication of COF nanosheets with high crystallinity is still challenging. Ahead of tedious and costly attempts in experiments, it is important to understand the rejection mechanism and thus screen the suitable COF materials with an outstanding permselectivity. Non-equilibrium molecular dynamics (NEMD) simulations are a powerful tool to investigate fluid transport through membranes. Prior works via NEMD simulations focus on salt rejection by investigating the effects of the pore size [24], layer number [25], staking fashion [26], and functionalization [27,28], which is important to the rational design of COF nanosheets for desalination. However, the potential of COF nanosheets on boron removal has not yet been investigated.

In this work, we expect to select a kind of COF with the pore size slightly larger than the size of $B(OH)_3$ but having a high affinity to water. This COF is expected to provide high water permeance due to the abundant water paths. To this end, a water-stable COF-TpTG with abundant carbonyl and amine groups inside nanopores was selected (Fig. 1a). Via NEMD simulations, the boron removal performance of the TpTG nanosheets with different numbers of layers is investigated. It is found that the TpTG multilayers show 100% $B(OH)_3$ rejection and excellent water permeance up to 276.7 L m^{-2} h^{-1} bar^{-1}, which is 2 orders of magnitude than traditional polyamide RO membranes.

2. Methods

2.1. Construction of models

Based on the experimental study, TpTG can be synthesized from the aldehyde precursor (1,3,5-triformylphloroglucinol, Tp) and the amino precursor (1,2,3-triaminoguanidine, TG) [29]. The monomeric unit is shown in Fig. 1a. The unit cell of TpTG was built based on $TpTG_{Cl}$ from the CoRE COF database [30]. It was then optimized by the Cambridge Sequential Total Energy Package (CASTEP) with the exchange-correlation functional of the general gradient approximation (GGA) formulated by Perdew-Burke-Ernzerhof (PBE). By extending the unit cell via periodical boundary conditions, we chose a TpTG fragment with twelve pores as the membrane model for the following molecular dynamics simulations (Fig. 1b).

Fig. 1c depicts water and $B(OH)_3$ molecules transport through the TpTG multilayers. The simulation system contains a feed chamber on the left side and a permeate chamber on the right side, which is separated by the TpTG membrane. The feed chamber with the boron concentration of 2.0 g L^{-1} contains 10 $B(OH)_3$ molecules solvated by 3000 water molecules. Following many simulation works [31–33], a much higher concentration than that of seawater (4.5 mg L^{-1}) was chosen to achieve sufficient statistics of $B(OH)_3$ transport events in the nanosecond timescale. The permeate chamber contains 607 water molecules. Moreover, two rigid graphene sheets at the ends of the system act as pistons to generate the desired pressures. The *x* and *y* dimensions of the simulation system are set to 3.61 and 3.12 nm, respectively, while the *z* dimension is changed with the membrane thickness.

2.2. Simulation methods

All the NEMD simulations were performed using the LAMMPS package [34]. The atom interactions are described by both the 12-6 Lennard-Jones (LJ) and the Coulombic potentials. The parameters for $B(OH)_3$ developed by Risplendi et al. [31] and the parameters for Na^+ and Cl^- proposed by Joung et al. [35] were used. To fit the models of $B(OH)_3$ and ions, the TIP4P-Ew water model [36] was adopted with the SHAKE algorithm which constrains the bonds and angles. The LJ interactions between the carbon atom of the graphene pistons and the oxygen atom of water were selected as the parameters: $\sigma_{C\text{-}O} = 0.319$ nm, $\varepsilon_{C\text{-}O} = 0.392$ kJ mol^{-1} [37]. The LJ parameters for the TpTG atoms were adopted from the Dreiding force field [38], which was widely used in the COF-based simulations [24,25,39]. The atomic partial charges of TpTG were described by electrostatic potential (ESP) charges, which were derived using the grid-based CHELPG algorithm based on density functional theory (DFT). The DFT calculations were performed at the B3LYP/6-311G(d,p) level with the Gaussian 09 package. The atomic partial charges were shown in Fig. S1 and Table S1 and S2. LJ cross-interaction parameters between different elements were based on the Lorentz-Berthelot combination rule. The cut-off distances of LJ and Coulombic interactions were set to 1.0 and 1.2 nm, respectively. The particle-particle particle-mesh (PPPM) method with the accuracy of 10^{-4} was used to calculate the long-range electrostatic interactions [40]. Periodic boundary conditions were only applied in *x* and *y* dimensions.

For each system, energy minimization was firstly performed with a

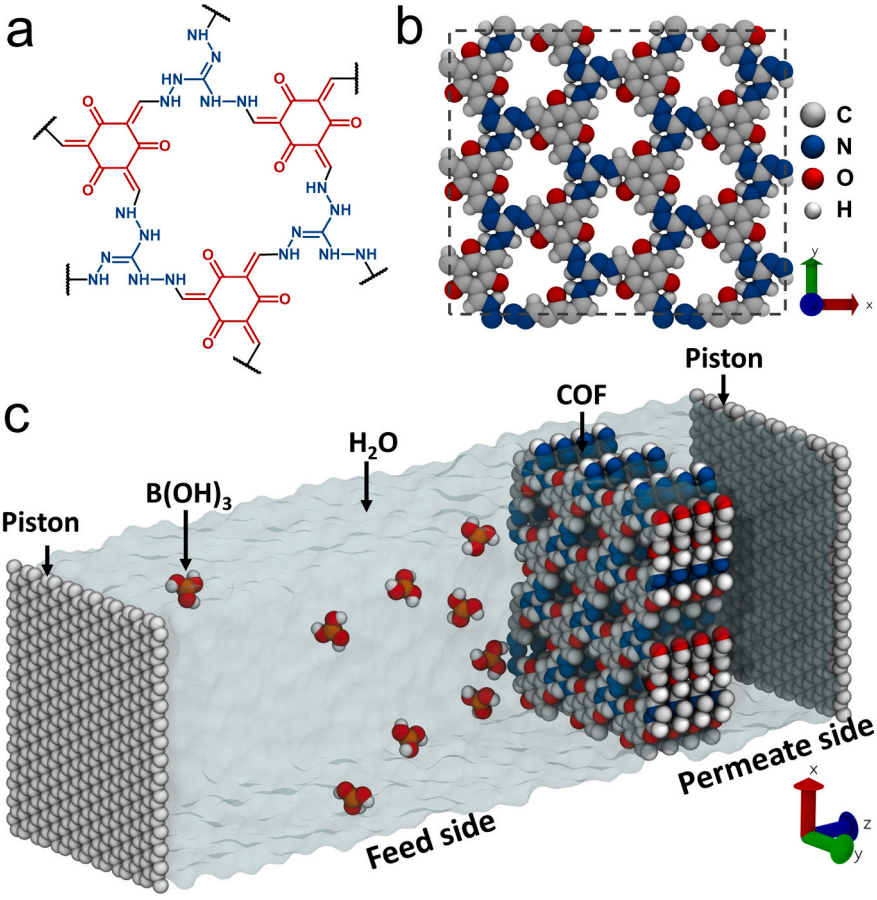

Fig. 1. (a) The monomeric unit of TpTG. (b) The periodic structure of TpTG. (c) Schematic of the simulation system for water and $B(OH)_3$ molecules transport through TpTG multilayers. The compositions are labeled in the figure.

tolerance of 10^{-5}. After that, a 2 ns equilibrium molecular dynamics simulation was performed at 300 K and 0.1 MPa to allow water molecules to wet the membranes. Finally, in the NEMD simulations, the external force (f) was applied to the atoms of the piston to generate the desired pressure (P):

$$P = \frac{nf}{A} \tag{1}$$

where n is the number of carbon atoms of the piston and A is the cross-sectional area of the membrane. Hence, the pressure drop (ΔP) across the membrane was generated as:

$$\Delta P = P_{feed} - P_{permeate} \tag{2}$$

where P_{feed} and $P_{permeate}$ represent the pressures on the feed and permeate pistons, respectively. P_{feed} was set to the desired pressure, and $P_{permeate}$ was set to 0.1 MPa (ambient pressure). The applied ΔP was set to 200 MPa that was much higher than the experimental conditions of several MPa. Such high ΔP is commonly used in NEMD simulations to enhance the signal-to-noise ratio within the nanosecond timescale [24,32,33]. The system temperature was kept at 300 K with the Nosé-Hoover thermostat. The trajectories were saved every 1 ps with a time step of 1 fs. Based on the water permeance performance of the TpTG membrane with different layers, the simulation time is ranged from 7 to 60 ns to allow half number of the water molecules (~1500) in the feed chamber to permeate through the membrane (Fig. S2). To reduce the statistical deviation, the results were obtained by taking an average of more than three separate runs with different initial configurations.

2.3. Post-simulation analysis

The linear increase in filtered water molecules with the sampling time indicates that the water flows reach a steady state (Fig. S2). The water flux was calculated by the slope of the number of water molecules filtered through the membrane with the sampling time. Moreover, the rejection (R) is calculated as:

$$R = 1 - \frac{c_p}{c_f} \tag{3}$$

where c_p and c_f are the $B(OH)_3$ concentrations in the permeate and feed solutions, respectively. The reliability of complete rejections to $B(OH)_3$ is demonstrated in Supplementary Material.

3. Results and discussion

3.1. Water permeance and boron rejection

After the NEMD simulations, the boron removal performance of the TpTG nanosheets was obtained at the beginning. Water permeance and $B(OH)_3$ rejection of the TpTG nanosheets are plotted as a function of the number of layers in Fig. 2a. Water permeance is sharply decreased from 1104 to 276.7 L m^{-2} h^{-1} bar^{-1} (LMHB) with increased layer number from 1 to 2, and then gradually decreased to 126.1 LMHB with layer number further increased to 5. The $B(OH)_3$ rejection undergoes a sharp increase from 64.2% to 100% with layer number increased from 1 to 2, and then maintains 100% with layer number further increased to 5. Strikingly, the TpTG bilayer achieves 100% $B(OH)_3$ rejection and the water permeance of 276.7 LMHB, which is 2 orders of magnitude higher

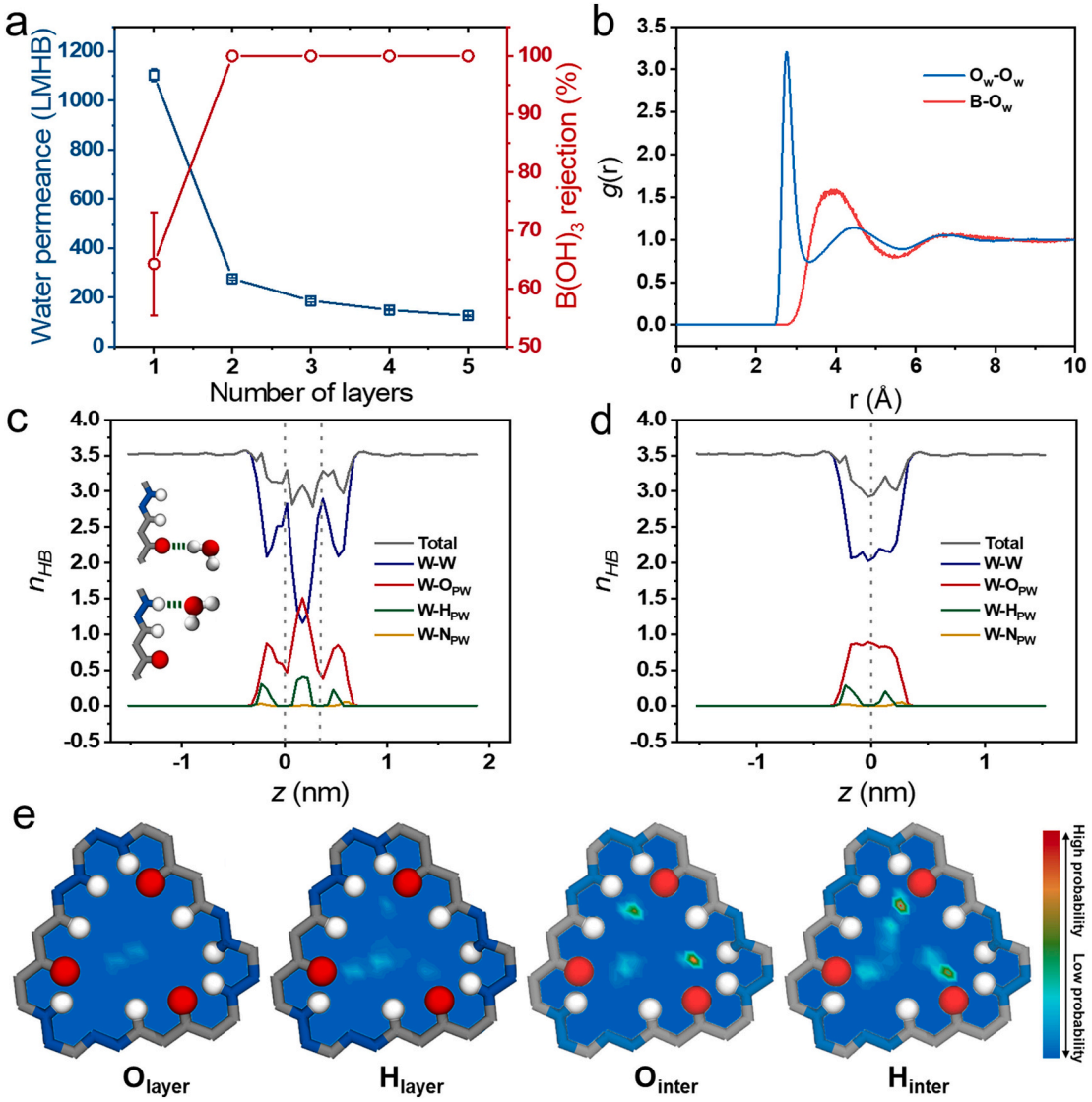

Fig. 2. (a) Water permeance and $B(OH)_3$ rejection as a function of the number of layers. (b) Radial distribution functions (RDFs) of the oxygen atom of water (O_w) and boron atom (B) with O_w. The average number of hydrogen bonds (n_{HB}) per water molecule along the *z*-direction of TpTG nanosheets with bilayer (c) and monolayer (d). HBs contain two parts: (i) HBs between water molecules (W-W); (ii) HBs between water and the atoms of the pore wall (PW), including oxygen, hydrogen, and nitrogen atoms (O_{PW}, H_{PW}, and N_{PW}, respectively). Total denotes n_{HB} of both these two parts. The insets are the illustration of HBs of water molecules with the oxygen and hydrogen atoms of the PW. The gray dashed lines represent the positions of the TpTG monolayers. (e) The *xy*-plane density maps for oxygen and hydrogen atoms of water in the layered (O_{layer}, H_{layer}) and interlayered (O_{inter}, H_{inter}) positions.

than the traditional RO membranes with >90% $B(OH)_3$ rejection [17–19]. Moreover, the simulation system for salty water transport through the TpTG monolayer was built (Fig. S4). It is found that the monolayer can achieve 100% NaCl rejection, which indicates the 100% NaCl rejections of the TpTG multilayers.

3.2. The rejection mechanism of boric acid

After revealing the excellent boron removal performance of the TpTG multilayer, we then investigate the mechanism of $B(OH)_3$ rejections. Our previous studies found that the rising ion rejection with the increased membrane thickness is due to the stronger dehydration of ions, which results in the promoted energy barrier [41]. Therefore, the hydration state of $B(OH)_3$ is then investigated by analyzing the radial distribution function (RDF). As shown in Fig. 2b, the first peak of the boron atom (B) with the oxygen atom of water (O_w) is much weaker at r = 4.0 Å, compared to the first peak of O_w with O_w at r = 2.8 Å. This observation indicates that the hydration shell of $B(OH)_3$ is much weaker than that of water, which is consistent with the previous study [42]. Unlike hydrated ions, due to the very weak hydration shell of $B(OH)_3$, there is no need for $B(OH)_3$ molecules to peel off the hydration shell when they try to enter the nanopores. Therefore, $B(OH)_3$ molecules will try to enter nanopores as single molecules without hydration, indicating the needlessness for investigating their dehydration effect.

We then consider the size of single molecules and the separation mechanism of the single-molecule sieving. The Stokes diameter of $B(OH)_3$, 3.1 Å, [14,43] is smaller than the pore diameter of TpTG which is 3.9 Å measured by the Zeo++ software [44]. Therefore, the single-molecule sieving mechanism cannot explain the moderate rejection of the monolayer and the complete rejection of the multilayers (Fig. 2a).

Inspired by the solution-diffusion model [45], we turn our attention to the selective separation based on the different membrane affinity to various species. As there are no $B(OH)_3$ molecules entering nanopores in TpTG multilayers because of the 100% rejections, we investigate the transport behaviors of water molecules inside nanopores. It was demonstrated that the transport behavior of confined water is highly

related to the formation and breaking of hydrogen bonds (HBs) [25,46]. Therefore, we plot the distribution of the average number of HBs (n_{HB}) per water molecule along the z-direction. The geometrical criterion is used to judge whether a HB exists [47]. The HB contribution contains two parts: (i) the HBs between water molecules; (ii) the HBs between water and the atoms of pore wall (PW), which compensates the loss of HBs between water molecules when they enter the nanopore, and this part is so-called the HB compensation. In the case of the TpTG bilayer (Fig. 2c), n_{HB} between water molecules is sharply decreased from 3.5 to 1.2 when water molecules transport from the bulk aqueous solution to the middle of the interlayer. At the same time, n_{HB}'s compensated by the oxygen and hydrogen atoms of PW are sharply increased from 0 to 1.5 and from 0 to 0.4, respectively. Taking the effect of HB compensations into consideration, the total n_{HB} undergoes a relatively slight decrease from 3.5 in the bulk aqueous solution to 2.8 in the middle of nanopores.

A similar HB compensation is also observed in the TpTG monolayer (Fig. 2d). By comparing the HB results for the monolayer and bilayer of TpTG, it is found that the loss of n_{HB} between water molecules and the HB compensations are most serious in the interlayer. To further measure the degree of HB compensations, an index named as the recovery rate of HB (*Rec*) is defined as n_{HB} between water and PW atoms divided by the lost part of n_{HB} between water molecules while entering the nanopore (see Supplementary Material for details). As shown in Fig. S5a, *Rec* is 60% in the TpTG monolayer, while it increases to 82% in the TpTG multilayers due to the strongest HB compensation in the interlayers. The HB loss between water molecules and the HB compensations indicate that water molecules need to rearrange their microstructure while entering nanopores, i.e., the HB rearrangement [48]. The HB rearrangement is the most serious in the interlayer, which results in a more ordered water structure inside the TpTG bilayer compared to the monolayer (Fig. S6). Besides, as shown in Fig. 2c-d, n_{HB} between water and the nitrogen atoms of PW is negligible, which is not further analyzed.

To further observe the water microstructure inside the TpTG nanopore, we then plot the *xy*-plane density maps for oxygen and hydrogen atoms of water in the layered and interlayered positions. As shown in Fig. 2e, the densities of oxygen and hydrogen atoms in the interlayers are much higher than those in the layered position. In the interlayers, the high-density areas of oxygen and hydrogen atoms are near the hydrogen and oxygen atoms of PW, respectively, which is due to the strongest HB compensation. Besides, water is in a three-chain arrangement near the inner pores, which is like the ordered water structure inside carbon nanotubes [49]. Moreover, the HB lifetime is calculated to prove that the HBs between water and PW atoms are stronger than HBs between water molecules in the bulk solution (Fig. S5b). Therefore, due to the HB interaction between water and the PW atoms, water preferentially adsorbs to the inner pore and occupies the nanopore. Consequently, the effective pore size for $B(OH)_3$ passage is about 2.1 Å, which can reject the $B(OH)_3$ molecule with the Stokes diameter of 3.1 Å (Fig. S7). Moreover, the strongest HB compensation in the interlayer explains why the rejection rapidly rises from 64.2% to 100% when the TpTG bilayer is placed.

Since both water and $B(OH)_3$ can form HBs, we then figure out why the membrane surface preferentially adsorbs water rather than $B(OH)_3$. The capabilities of $B(OH)_3$ and water to form HBs in the bulk aqueous solutions were separately investigated. In the bulk aqueous solutions, as shown in Fig. 3a, n_{HB}'s per $B(OH)_3$ molecule as a donor and an acceptor are 1.5 and 0.7, respectively, while n_{HB}'s per water molecule as a donor and an acceptor are both 1.8. The HB numbers between $B(OH)_3$ and water molecules are less than that between water and water molecules.

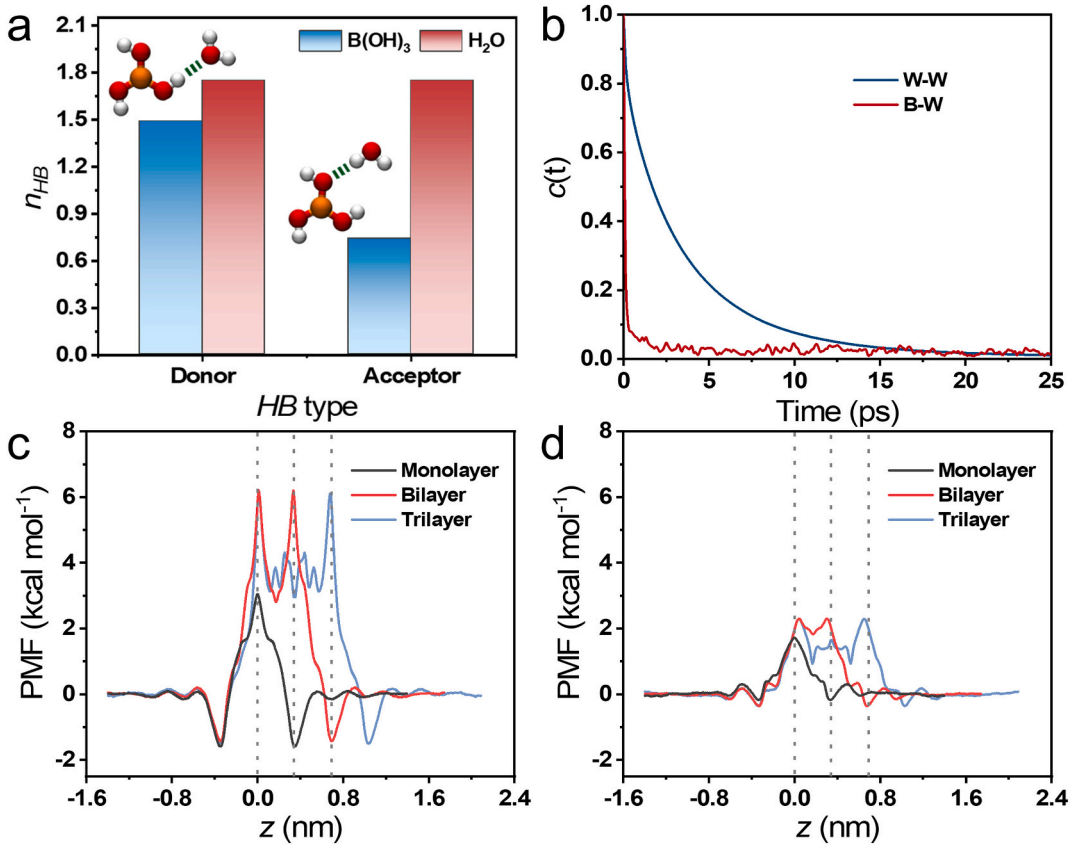

Fig. 3. (a) n_{HB} per molecule for $B(OH)_3$ and water in the form of donor and acceptor in bulk aqueous solutions. The insets are the illustration of $B(OH)_3$ as a donor (left) and an acceptor (right), respectively. (b) HB autocorrelation functions for water-water (W—W) and $B(OH)_3$-water (B—W). The PMFs for $B(OH)_3$ (c) and water (d) transport through TpTG nanosheets with different numbers of layers. The gray dashed lines represent the positions of the TpTG monolayers.

Besides, $B(OH)_3$ preferentially donates rather than accepts HBs, which is consistent with the reported literature [31]. Moreover, compared to HBs between water and water molecules (W—W), the decrease in the HB autocorrelation function for the HBs between $B(OH)_3$ and water (B—W) is faster (Fig. 3b), which indicates that HBs are weaker between $B(OH)_3$ and water. Therefore, the fewer HB numbers and the weaker HB strength between $B(OH)_3$ and water mean that the capability of water to form HBs is better than that of $B(OH)_3$. Furthermore, because water molecule has a smaller size and a better capability to form HBs compared to $B(OH)_3$ molecule, the TpTG nanopore will preferentially adsorb water to form more HBs, which consequently lowers the free energy of the system.

To further investigate the free energy barriers for molecules passing through the TpTG nanopore, the potential of mean forces (PMFs) were calculated. The PMFs for $B(OH)_3$ and water were calculated using the umbrella sampling method (see Supplementary Material for details), and the whole reaction coordinate was sampled well (Fig. S8). The PMFs for $B(OH)_3$ passage along the *z*-direction in TpTG nanopores with the different numbers of layers are shown in Fig. 3c. In the TpTG monolayer, the PMFs for the $B(OH)_3$ in the bulk aqueous solution are zero as a reference and sharply increase to 3.0 kcal mol^{-1} in the middle of the nanopore. With the layer number tuning from 1 to 2, the energy barrier for $B(OH)_3$ is increased from 3.0 to 6.2 kcal mol^{-1}. With the layer number further increased to 3, the PMF maintains 6.2 kcal mol^{-1}. The PMFs for $B(OH)_3$ are maximized at the entrance/exit because $B(OH)_3$ needs to push the adsorbed water away, and are relatively decreased inside the pore due to the HB interaction between $B(OH)_3$ and the PW atoms.

The PMFs for water are shown in Fig. 3d. The PMFs for water have local minimums in the interlayers because of the HB interaction between water and the PW atoms. In the case of the TpTG monolayer, the PMFs for water are much lower compared to $B(OH)_3$, which results in the rejection to $B(OH)_3$. The difference in the energy barrier between $B(OH)_3$ and water is evidently promoted when the bilayer replaces the monolayer, leading to the enhanced $B(OH)_3$ rejections. With the layer number further increased from 2 to 3, this difference is nearly unchanged, and thus the $B(OH)_3$ rejection maintains unchanged.

3.3. Eliminating the effect of hydrogen bonding compensation

To further verify that the strong surface affinity to water results from the HB effect, we modified the nanopore to eliminate or weaken the effect of HB compensation of PW. As shown in Fig. 4a, two methods were proposed. One method is to remove all the partial atomic charges of the TpTG pore to construct an apolar TpTG pore, which has the same pore size as the normal TpTG pore but cannot form HBs with water molecules. Another method is based on experiments [50]. By the introduction of three methoxy ($-OCH_3$) groups adjacent to the aldehyde (-CHO) groups in the aldehyde building unit, the pore size of the nanopore becomes slightly smaller and the effect of HB compensation of PW atoms is greatly weakened simultaneously. Herein, the functional $-OCH_3$ at the edge of nanopores was set to be flexible.

The boron removal performances of the apolar TpTG and TpOMe-TG were then investigated. As shown in Fig. 4b, compared to the high rejections of the normal TpTG, the $B(OH)_3$ rejections of the apolar TpTG with monolayer and bilayer are both nearly 0%. Since they have the same pore size, it is demonstrated that the effect of the size exclusion is negligible. Moreover, the $B(OH)_3$ rejections of the TpOMe-TG monolayer and bilayer are only 7.4% and 13.2%, respectively. In the absence of the HB interaction between water and the PW atoms, even a nanopore with a smaller pore size will obtain a lower rejection to $B(OH)_3$.

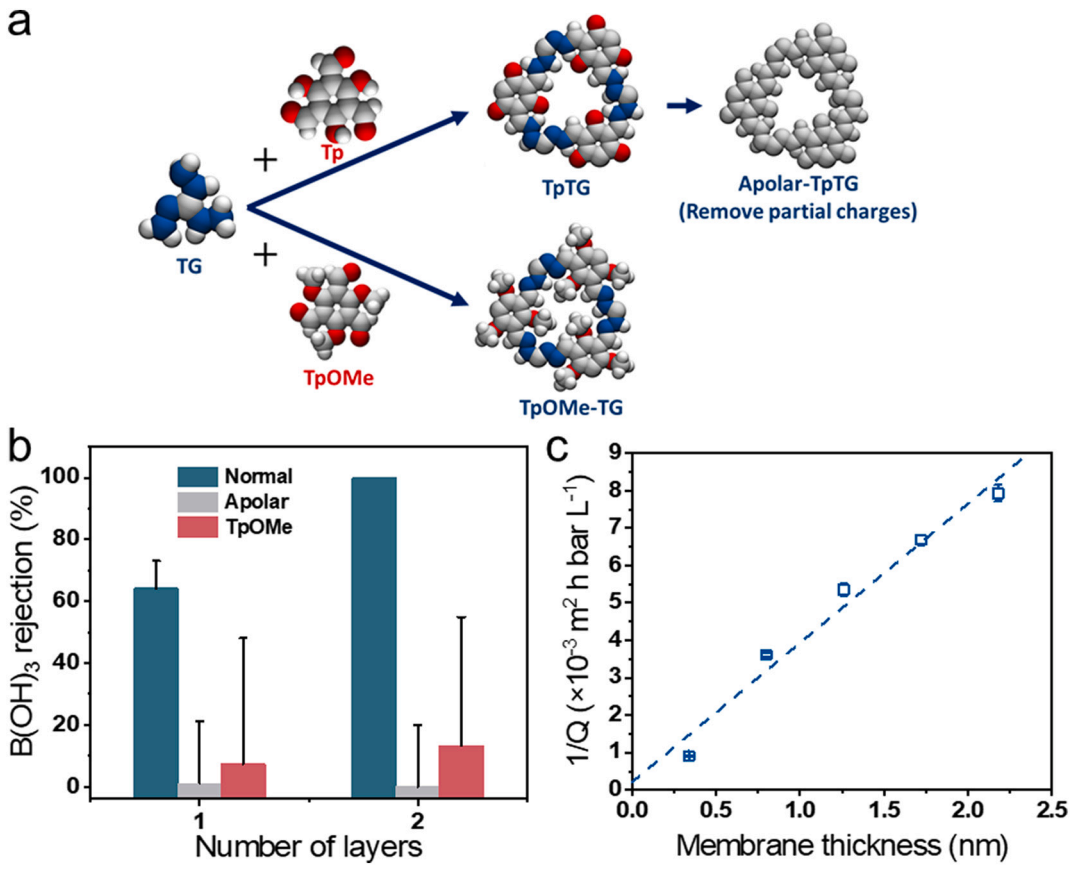

Fig. 4. (a) Schematics for the normal TpTG, the apolar TpTG, and the TpOMe-TG. (b) The $B(OH)_3$ rejections of these three membranes with different numbers of layers. (c) The reciprocal of water permeance (1/Q) as a function of membrane thicknesses.

3.4. Water permeance at real-world thicknesses

Finally, water permeance of the TpTG nanosheets of a real-world RO membrane thickness was investigated. In our previous studies [25,26,51], the total transport resistance (R_{total}) was divided into two parts, including the interior and the interfacial contributions. R_{total} can be calculated as:

$$R_{total} = \frac{\Delta P}{J} = \frac{\mu}{\kappa \pi r^2} l_{mem} + \frac{\mu C}{r^3} \quad (4)$$

where J is the water flux; μ is the dynamic viscosity of water in the nanopore; κ is the intrinsic permeability of the membrane; r is the pore radius; l_{mem} is the membrane thickness; C is the loss coefficient, a constant value that is related to the physical and chemical properties of the membrane. $\frac{\mu}{\kappa \pi r^2} l_{mem}$ represents the interior resistance that obeys Darcy's law [47], $\frac{\mu C}{r^3}$ represents the interfacial resistance that obeys the Sampson's equation [52,53]. Besides, as water permeance (Q) is equal to $J/\Delta P$, the relationship between Q and l_{mem} is established:

$$\frac{1}{Q} = \frac{\mu}{\kappa \pi r^2} l_{mem} + \frac{\mu C}{r^3} \quad (5)$$

As shown in Fig. 4c, by making a linear fitting between the reciprocal water permeance (1/Q) and l_{mem}, a quantitative equation is established:

$$\frac{10^3}{Q} = 3.723 l_{mem} + 0.209 \quad (6)$$

The units of Q and l_{mem} are LMHB and nm, respectively. Form Eq. (6), the value of the slope ($\frac{\mu}{\kappa \pi r^2} = 3.723$) is much higher than that of the intercept ($\frac{\mu C}{r^3} = 0.2090$), which results in a rapidly increased interior resistance with increased l_{mem}, which is because the HB interaction between water and PW atoms leads to significant friction. Based on Eq. (6), water permeance at a real-world RO membrane thickness of 20 nm [54,55] can be extrapolated. The calculated water permeance is 13.4 LMHB, which is 1 order of magnitude higher than that of reported polyamide membranes with >90% boron rejections [17–19]. Such high water permeance results from the three-chain structure that allows sufficient water channels (Fig. 2e), even though the transport resistance is significant due to the HB interaction between water and the PW atoms. Moreover, the main advantage of the TpTG membrane may be its thinness as two or a few layers will obtain ultrahigh water permeance and complete $B(OH)_3$ rejections.

4. Conclusions

Via NEMD simulations, we show that the $B(OH)_3$ rejection is 64.2% in the TpTG monolayer and increases to 100% in the TpTG multilayers with excellent water permeance. Since $B(OH)_3$ is found to have weak hydration shells and its Stokes diameter of 3.1 Å is smaller than the pore diameter of 3.9 Å, the high $B(OH)_3$ rejections should be attributed to the mechanism other than the size exclusion. Based on the analysis of water microstructure inside nanopores, it is found that the hydrogen bonding (HB) interaction between water and the atoms of the pore wall (PW) rearranges water molecules to a three-chain structure. This HB compensation of PW facilitates the preferential adsorption of water into the nanopore, and the occupied water molecules will impede the $B(OH)_3$ passage. The HB compensation is strongest in the interlayers, leading to a higher $B(OH)_3$ rejection in TpTG multilayers. Moreover, when the HB effect between water and the PW atoms is eliminated or weakened, the modified nanopores show very low $B(OH)_3$ rejections, which confirms the key role of the HB compensation for boron removal. Furthermore, the three-chain water structure allows high water permeance of 13.4 L m^{-2} h^{-1} bar^{-1} (LMHB) at a real-world thickness of 20 nm, which is 1 order of magnitude higher than the traditional RO membranes. If the TpTG membrane can be prepared as a bilayer, the water permeance will be as high as 276.7 LMHB. This work is expected to be helpful to the rational design of desalination membranes with high boron rejections and upgraded water permeance. The proposed preferential adsorption mechanism may be applied for the removal of many other small neutral solutes such as *N*-nitrosodimethylamine, a disinfection byproduct.

CRediT authorship contribution statement

Xin Zhang: Conceptualization, Investigation, Methodology, Software, Formal analysis, Validation, Writing - original draft. **Mingjie Wei**: Methodology, Writing - review & editing, Data curation, Visualization, Funding acquisition. **Zhe Zhang**: Writing - review & editing. **Xiansong Shi**: Writing - review & editing. **Yong Wang**: Writing - review & editing, Supervision, Funding acquisition.

Declaration of competing interest

The authors declare that they have no known competing financial interests or personal relationships that could have appeared to influence the work reported in this paper.

Acknowledgments

Financial support from the National Natural Science Foundation of China (21825803, 21921006) and the Jiangsu Natural Science Foundation (BK20190085). We thank the High Performance Computing Center of Nanjing Tech University for supporting the computational resources. We are also grateful to the Program of Excellent Innovation Teams of Jiangsu Higher Education Institutions and the Project of Priority Academic Program Development of Jiangsu Higher Education Institutions (PAPD).

Appendix A. Supplementary data

Atomic partial charges for the TpTG and TpOMe-TG, steady-state water flows and reliability of complete rejections, the NaCl rejection of the TpTG monolayer, the recovery rate of HB and HB autocorrelation functions, the dipole orientation of water inside pores, illustration of effective pore size for $B(OH)_3$ passage, and calculation details of the potential of mean force (PMF). Supplementary data to this article can be found online at https://doi.org/10.1016/j.desal.2022.115548.

References

[1] E. Jones, M. Qadir, M.T.H. van Vliet, V. Smakhtin, S.-M. Kang, The state of desalination and brine production: a global outlook, Sci. Total Environ. 657 (2019) 1343–1356, https://doi.org/10.1016/j.scitotenv.2018.12.076.
[2] J.R. Werber, C.O. Osuji, M. Elimelech, Materials for next-generation desalination and water purification membranes, Nat. Rev. Mater. 1 (2016) 16018, https://doi.org/10.1038/natrevmats.2016.18.
[3] J.R. Werber, A. Deshmukh, M. Elimelech, The critical need for increased selectivity, not increased water permeability, for desalination membranes, Environ. Sci. Technol. Lett. 3 (2016) 112–120, https://doi.org/10.1021/acs.estlett.6b00050.
[4] A.D. Nikolaou, S.K. Golfinopoulos, G.B. Arhonditsis, V. Kolovoyiannis, T.D. Lekkas, Modeling the formation of chlorination by-products in river waters with different quality, Chemosphere 55 (2004) 409–420, https://doi.org/10.1016/j.chemosphere.2003.11.008.
[5] F.S. Kot, Boron in the environment, Boron Sep. Process. (2015) 1–33, https://doi.org/10.1016/B978-0-444-63454-2.00001-0.
[6] Z. Guan, J. Lv, P. Bai, X. Guo, Boron removal from aqueous solutions by adsorption-a review, Desalination 383 (2016) 29–37, https://doi.org/10.1016/j.desal.2015.12.026.
[7] B. Wang, X. Guo, P. Bai, Removal technology of boron dissolved in aqueous solutions-a review, Colloids Surf. A Physicochem. Eng. Asp. 444 (2014) 338–344, https://doi.org/10.1016/j.colsurfa.2013.12.049.
[8] F. Edition, Guidelines for drinking-water quality, WHO Chron. 38 (2011) 104–108.
[9] N. Hilal, G. Kim, C. Somerfield, Boron removal from saline water: a comprehensive review, Desalination 273 (2011) 23–35, https://doi.org/10.1016/j.desal.2010.05.012.
[10] Z. Ali, Y. Al Sunbul, F. Pacheco, W. Ogieglo, Y. Wang, G. Genduso, I. Pinnau, Defect-free highly selective polyamide thin-film composite membranes for

desalination and boron removal, J. Membr. Sci. 578 (2019) 85–94, https://doi.org/10.1016/j.memsci.2019.02.032.
[11] A. Farhat, F. Ahmad, N. Hilal, H.A. Arafat, Boron removal in new generation reverse osmosis (RO) membranes using two-pass RO without pH adjustment, Desalination 310 (2013) 50–59, https://doi.org/10.1016/j.desal.2012.10.003.
[12] O. Nir, O. Lahav, Single SWRO pass boron removal at high pH: prospects and challenges, in: Boron Separation Processes, Elsevier, Haifa, Israel, 2015, pp. 297–323.
[13] Y.P. Tang, L. Luo, Z. Thong, T.S. Chung, Recent advances in membrane materials and technologies for boron removal, J. Membr. Sci. 541 (2017) 434–446, https://doi.org/10.1016/j.memsci.2017.07.015.
[14] R. Bernstein, S. Belfer, V. Freger, Toward improved boron removal in RO by membrane modification: feasibility and challenges, Environ. Sci. Technol. 45 (2011) 3613–3620, https://doi.org/10.1021/es103991u.
[15] S. Shultz, V. Freger, In situ modification of membrane elements for improved boron rejection in RO desalination, Desalination 431 (2018) 66–72, https://doi.org/10.1016/j.desal.2017.08.021.
[16] S. Shultz, M. Bass, R. Semiat, V. Freger, Modification of polyamide membranes by hydrophobic molecular plugs for improved boron rejection, J. Membr. Sci. 546 (2018) 165–172, https://doi.org/10.1016/j.memsci.2017.10.003.
[17] S. Wang, Y. Zhou, C. Gao, Novel high boron removal polyamide reverse osmosis membranes, J. Membr. Sci. 554 (2018) 244–252, https://doi.org/10.1016/j.memsci.2018.03.014.
[18] Y. Li, S. Wang, X. Song, Y. Zhou, H. Shen, X. Cao, P. Zhang, C. Gao, High boron removal polyamide reverse osmosis membranes by swelling induced embedding of a sulfonyl molecular plug, J. Membr. Sci. 597 (2020), 117716, https://doi.org/10.1016/j.memsci.2019.117716.
[19] L. Liu, X. Xie, S. Qi, R. Li, X. Zhang, X. Song, C. Gao, Thin film nanocomposite reverse osmosis membrane incorporated with UiO-66 nanoparticles for enhanced boron removal, J. Membr. Sci. 580 (2019) 101–109, https://doi.org/10.1016/j.memsci.2019.02.072.
[20] M. Di Vincenzo, M. Barboiu, A. Tiraferri, Y. Legrand, Polyol-functionalized thin-film composite membranes with improved transport properties and boron removal in reverse osmosis, J. Membr. Sci. 540 (2017) 71–77, https://doi.org/10.1016/j.memsci.2017.06.034.
[21] H.B. Park, J. Kamcev, L.M. Robeson, M. Elimelech, B.D. Freeman, Maximizing the right stuff: the trade-off between membrane permeability and selectivity, Science 356 (2017), eaab0530, https://doi.org/10.1126/science.aab0530.
[22] A. Sagiv, R. Semiat, Analysis of parameters affecting boron permeation through reverse osmosis membranes, J. Membr. Sci. 243 (2004) 79–87, https://doi.org/10.1016/j.memsci.2004.05.029.
[23] Y. Lan, X. Han, M. Tong, H. Huang, Q. Yang, D. Liu, X. Zhao, C. Zhong, Materials genomics methods for high-throughput construction of COFs and targeted synthesis, Nat. Commun. 9 (2018) 1–10, https://doi.org/10.1038/s41467-018-07720-x.
[24] L.C. Lin, J. Choi, J.C. Grossman, Two-dimensional covalent triazine framework as an ultrathin-film nanoporous membrane for desalination, Chem. Commun. 51 (2015) 14921–14924, https://doi.org/10.1039/C5CC05969K.
[25] W. Zhou, M. Wei, X. Zhang, F. Xu, Y. Wang, Fast desalination by multilayered covalent organic framework (COF) nanosheets, ACS Appl. Mater. Interfaces 11 (2019) 16847–16854, https://doi.org/10.1021/acsami.9b01883.
[26] M. Wei, W. Zhou, F. Xu, Y. Wang, Nanofluidic behaviors of water and ions in covalent triazine framework (CTF) multilayers, Small (2019), https://doi.org/10.1002/smll.201903879, 1903879.
[27] K. Zhang, Z. He, K.M. Gupta, J. Jiang, Computational design of 2D functional covalent–organic framework membranes for water desalination, Environ. Sci. Water Res. Technol. 3 (2017) 735–743, https://doi.org/10.1039/C7EW00074J.
[28] F. Xu, M. Wei, Y. Wang, Effect of hydrophilicity on ion rejection of sub-nanometer pores, Sep. Purif. Technol. 257 (2021), 117937, https://doi.org/10.1016/j.seppur.2020.117937.
[29] S. Mitra, S. Kandambeth, B.P. Biswal, C.K. Choudhury, M. Mehta, G. Kaur, S. Banerjee, A. Prabhune, S. Verma, A.M. Khayum, Self-exfoliated guanidinium-based ionic covalent organic nanosheets (iCONs), J. Am. Chem. Soc. 138 (2016) 2823–2828, https://doi.org/10.1021/jacs.5b13533.
[30] M. Tong, Y. Lan, Q. Yang, C. Zhong, Exploring the structure-property relationships of covalent organic frameworks for noble gas separations, Chem. Eng. Sci. 168 (2017) 456–464, https://doi.org/10.1016/j.ces.2017.05.004.
[31] F. Risplendi, F. Raffone, L.-C. Lin, J.C. Grossman, G. Cicero, Fundamental insights on hydration environment of boric acid and its role in separation from saline water, J. Phys. Chem. C 124 (2019) 1438–1445, https://doi.org/10.1021/acs.jpcc.9b10065.
[32] Z. Cao, V. Liu, A., Barati farimani, water desalination with two-dimensional metal-organic framework membranes, Nano Lett. 19 (2019) 8638–8643, https://doi.org/10.1021/acs.nanolett.9b03225.
[33] M. Heiranian, A.B. Farimani, N.R. Aluru, Water desalination with a single-layer MoS2 nanopore, Nat. Commun. 6 (2015) 8616, https://doi.org/10.1038/ncomms9616.
[34] S. Plimpton, Fast parallel algorithms for short-range molecular dynamics, J. Comput. Phys. 117 (1995) 1–19, https://doi.org/10.1006/jcph.1995.1039.
[35] I.S. Joung, T.E. Cheatham, Determination of alkali and halide monovalent ion parameters for use in explicitly solvated biomolecular simulations, J. Phys. Chem. B 112 (2008) 9020–9041, https://doi.org/10.1021/jp8001614.
[36] H.W. Horn, W.C. Swope, J.W. Pitera, J.D. Madura, T.J. Dick, G.L. Hura, T. Head-Gordon, Development of an improved four-site water model for biomolecular simulations: TIP4P-ew, J. Chem. Phys. 120 (2004) 9665–9678, https://doi.org/10.1063/1.1683075.
[37] T. Werder, J. Walther, R. Jaffe, T. Halicioglu, P. Koumoutsakos, On the water-carbon interaction for use in molecular dynamics simulations of graphite and carbon nanotubes, J. Phys. Chem. B 107 (2003) 1345–1352, https://doi.org/10.1021/jp0268112.
[38] S.L. Mayo, B.D. Olafson, W.A. Goddard, DREIDING: a generic force field for molecular simulations, J. Phys. Chem. 94 (1990) 8897–8909, https://doi.org/10.1021/j100389a010.
[39] M. Tong, Q. Yang, Y. Xiao, C. Zhong, Revealing the structure-property relationship of covalent organic frameworks for CO2 capture from postcombustion gas: a multi-scale computational study, Phys. Chem. Chem. Phys. 16 (2014) 15189–15198, https://doi.org/10.1039/C4CP02047B.
[40] T. Darden, D. York, L. Pedersen, Particle mesh ewald: an N· log (N) method for ewald sums in large systems, J. Chem. Phys. 98 (1993) 10089–10092, https://doi.org/10.1063/1.464397.
[41] X. Zhang, M. Wei, F. Xu, Y. Wang, Thickness-dependent ion rejection in nanopores, J. Membr. Sci. 601 (2020), 117899, https://doi.org/10.1016/j.memsci.2020.117899.
[42] Y. Zhou, T. Yamaguchi, W. Zhang, K. Ikeda, K. Yoshida, F. Zhu, H. Liu, The structural elucidation of aqueous H_3BO_3 solutions by DFT and neutron scattering studies, Phys. Chem. Chem. Phys. 22 (2020) 17160–17170, https://doi.org/10.1039/D0CP02306J.
[43] J.K. Park, K.J. Lee, Diffusion coefficients for aqueous boric acid, J. Chem. Eng. Data 39 (1994) 891–894, https://doi.org/10.1021/je00016a057.
[44] T.F. Willems, C.H. Rycroft, M. Kazi, J.C. Meza, M. Haranczyk, Algorithms and tools for high-throughput geometry-based analysis of crystalline porous materials, Micropor. Mesopor. Mat. 149 (2012) 134–141, https://doi.org/10.1016/j.micromeso.2011.08.020.
[45] J.G. Wijmans, R.W. Baker, The solution-diffusion model: a review, J. Membr. Sci. 107 (1995) 1–21, https://doi.org/10.1016/0376-7388(95)00102-I.
[46] N. Zhang, S. Chen, B. Yang, J. Huo, X. Zhang, J. Bao, X. Ruan, G. He, Effect of hydrogen-bonding interaction on the arrangement and dynamics of water confined in a polyamide membrane: a molecular dynamics simulation, J. Phys. Chem. B 122 (2018) 4719–4728, https://doi.org/10.1021/acs.jpcb.7b12790.
[47] J. Muscatello, F. Jaeger, O.K. Matar, E.A. Müller, Optimizing water transport through graphene-based membranes: insights from nonequilibrium molecular dynamics, ACS Appl. Mater. Interfaces 8 (2016) 12330–12336, https://doi.org/10.1021/acsami.5b12112.
[48] R.H. Tunuguntla, R.Y. Henley, Y.-C. Yao, T.A. Pham, M. Wanunu, A. Noy, Enhanced water permeability and tunable ion selectivity in subnanometer carbon nanotube porins, Science 357 (2017) 792–796, https://doi.org/10.1126/science.aan2438.
[49] J.A. Thomas, A.J. McGaughey, Water flow in carbon nanotubes: transition to subcontinuum transport, Phys. Rev. Lett. 102 (2009), 184502, https://doi.org/10.1103/PhysRevLett.102.184502.
[50] A. Halder, S. Karak, M. Addicoat, S. Bera, A. Chakraborty, S.H. Kunjattu, P. Pachfule, T. Heine, R. Banerjee, Ultrastable imine-based covalent organic frameworks for sulfuric acid recovery: an effect of interlayer hydrogen bonding, Angew. Chem. Int. Edit. 57 (2018) 5797–5802, https://doi.org/10.1002/anie.201802220.
[51] X. Zhang, W. Zhou, F. Xu, M. Wei, Y. Wang, Resistance of water transport in carbon nanotube membranes, Nanoscale 10 (2018) 13242–13249, https://doi.org/10.1039/C8NR03116A.
[52] R.A. Sampson, On Stokes's current function, Philos. Trans. R. Soc., A (1891) 449–518, https://doi.org/10.1098/rsta.1891.0012.
[53] M.E. Suk, Narayana R. Aluru, Modeling water flow through carbon nanotube membranes with entrance/exit effects, Nanoscale Microscale Thermophys. Eng. 21 (2017) 247–262, https://doi.org/10.1080/15567265.2017.1355949.
[54] H. Yan, X. Miao, J. Xu, G. Pan, Y. Zhang, Y. Shi, M. Guo, Y. Liu, The porous structure of the fully-aromatic polyamide film in reverse osmosis membranes, J. Membr. Sci. 475 (2015) 504–510, https://doi.org/10.1016/j.memsci.2014.10.052.
[55] F. Pacheco, R. Sougrat, M. Reinhard, J.O. Leckie, I. Pinnau, 3D visualization of the internal nanostructure of polyamide thin films in RO membranes, J. Membr. Sci. 501 (2016) 33–44, https://doi.org/10.1016/j.memsci.2015.10.061.